AIAA AVIATION Forum
12-16 June 2023, San Diego, CA and Online
AIAA AVIATION 2023 Forum

10.2514/6.2023-4240

Experimental Investigation of a High-Frequency Pulsed Supersonic Co-Axial Injector using Optical Diagnostics

Jacob E. Jenkins* and Phillip A. Kreth†
University of Tennessee Space Institute, Tullahoma, TN, 37388

John T. Solomon‡
Tuskegee University, Tuskegee, AL, 36088

With an increased national emphasis on the development of high-speed systems, especially those utilizing air-breathing propulsion, there is a strong demand for efficient means of enhancing the mixing of fuel injection and an air stream that may be moving at supersonic speeds. In recent years, small scale fluidic-based actuators have shown promise in their ability promote efficient mixing in these scenarios due to their small size and having no moving parts. High-frequency pulsed co-axial actuators developed at Tuskegee University are one such device that only rely on a compressed gas source and particular geometric designs to enable rapid pulsed injection. These actuators are able to efficiently atomize injected fluids, such as fuels or oxidizers, and they can be designed to pulse at frequencies in excess of 15 kHz. This paper presents the results of an experimental investigation of one such device using advanced optical and laser diagnostics to measure both the spectral content and the unsteady velocity fields of the pulsed jet output. The flowfield is visualized with high-speed schlieren imaging, and the near-field acoustic emission is measured by a microphone. Focused laser differential interferometry (FLDI) and planar particle image velocimetry (PIV) are conducted within the actuator's pulsed jet output. The spectral content measured from FLDI closely matches the acoustic spectra. While the phase-locked velocity fields demonstrate the pulsing behavior of the actuator's core flow jet, the calculated velocities appear to be lower than what was anticipated based on inspection of the high-speed schlieren images. Velocity fields are presented for the actuator operating in both steady and pulsed modes of operation, and the results indicate that the pulsed actuation jet has the potential to significantly enhance mixing of the annular stream when it is introduced.

Downloaded by John Solomon on July 15, 2023 | http://arc.aiaa.org | DOI: 10.2514/6.2023-4240

I. Introduction

Flow control and fluid mixing in high-speed cross-flows have been studied for several decades due to their direct applications such as air breathing combustion systems. The use of small-scale actuating jets has proven to be a well characterized method for flow control, and such devices have been developed to complement the mixing of two different fluids [1]. Researchers at Tuskegee University [1] have developed co-axial injectors that produce a gaseous core flow which pulses at ultra-high frequencies (in excess of 15 kHz) and over a wide range of velocities (from sub- to supersonic). Surrounding this core flow, an annular jet can inject a steady stream of a fluid which would typically be the fuel or liquid oxidizer. When the two streams meet, the central jet's pulsed behavior produces a compressible vortex that interacts with the annular stream and creates a highly-atomized flow [1]. The core flow region pulsates as a result of a flow-acoustic resonance that exists between an external underexpanded source jet (with a 1.5 mm inner diameter in the present study) that flows into and interacts with a cylindrical cavity upstream of the core flow orifice. By appropriately sizing the cylindrical cavity, the source jet, and the exit orifices, the pulsing frequency of these actuators can be varied over a wide range [2]. Figure 1 shows the geometric details and an illustrative schematic of the flowfield for the actuator used in this study. The source jet impingement on the cylindrical cavity creates the resonance and provides fluid for the core flow, while a separate supply can be connected to the annular nozzle which is designed to eject a steady stream of fluid around the pulsed core flow.

The results collected in the present study are focused on the flow phenomena associated with the pulsing core flow jet alone (i.e., there is no co-axial injection in these experiments). The unsteady core flow jet governs the atomization

*Graduate Research Assistant, Department of Mechanical, Aerospace, and Biomedical Engineering, Student Member AIAA.
†Assistant Professor, Department of Mechanical, Aerospace, and Biomedical Engineering, Senior Member AIAA.
‡Associate Professor, Department of Mechanical Engineering, Senior Member AIAA.

Copyright © 2023 by The authors. Published by the American Institute of Aeronautics and Astronautics, Inc., with permission.

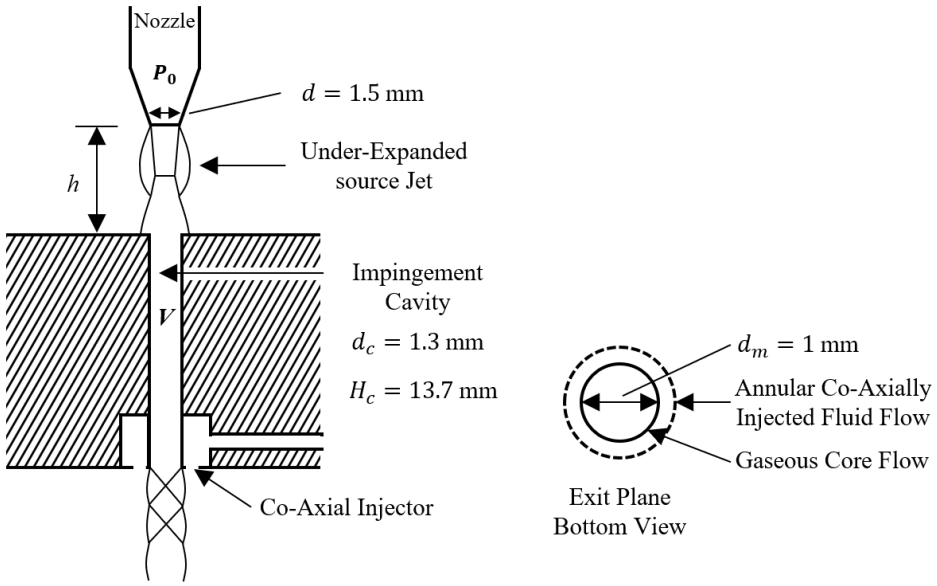

Fig. 1 Geometric and flowfield schematic of the high-frequency pulsed supersonic co-axial injector.

Downloaded by John Solomon on July 15, 2023 | http://arc.aiaa.org | DOI: 10.2514/6.2023-4240

of the co-axially-injected fluid and must be well-understood to enable detailed investigations of the multi-stream / multi-phase combined flow. The pulsed jet frequency can be varied over a narrow range for a particular design by varying one of two non-dimensional parameters: the distance between the source jet and cylindrical cavity, h/d, and the nozzle pressure ratio, NPR, which is the ratio of the source jet stagnation pressure to the ambient pressure [2]. For these actuators, the diameter used to non-dimensionalize the distance is the source jet inner diameter, d, which is 1.5 mm for the present configuration. At a given h/d, there is a small range for NPR over which the actuator will pulse. This is due to the unsteady interaction that the underexpanded source jet has with the cavity it impinges upon. Outside of this range, the actuator will produce a steady exit jet which can be supersonic under certain conditions. Typically, the NPR required for the actuator to pulse at high-frequencies increases with the selected h/d. In this study, results have been compiled for an actuator operating at design conditions of h/d = 1.8 and NPR = 4.9 (57 psig). Under these conditions, the actuator resonates at approximately 19 kHz.

Previous studies on similar microactuators have used more traditional methods such as microphones and unsteady pressure transducers to characterize the acoustic and pressure spectra [3], though high-magnification phase-locked particle image velocimetry (PIV) has been used to measure the velocity fields [4]. The current study utilizes high-speed schlieren imaging, focused laser differential interferometry (FLDI), and PIV to characterize various aspects of the co-axial injector's flowfield, with only the core flow jet operating in both a steady and pulsed mode. The results from these advanced optical and laser diagnostic techniques are compared to one another, and good agreement of the results is observed. Focused laser differential interferometry (FLDI) is an interferometric technique which uses a focused He-Ne laser beam to detect density disturbances within the pulsing core flow exiting the actuator, as shown in related efforts by Gragston, et al. [5] and Price, et al. [6]. FLDI is used to measure the spectral content of the pulsed jet, and comparisons are made to the acoustic spectra measured with a microphone in the near-field. The signals from a multi-point FLDI implementation are used to estimate the convective velocities along the jet centerline. Direct velocity measurements of the actuator's output are conducted in a separate configuration using phase-locked, planar particle image velocimetry (PIV).

II. Experimental Details

A. The Tuskegee University Co-Axial Injector

Figure 2 shows a detailed drawing (including the relevant internal dimensions) of the high-frequency, pulsed, supersonic co-axial actuator provided by Tuskegee University. The internal cavity is 13.7 mm long and has an initial diameter of 1.3 mm that is narrowed down to 1 mm at the exit (the bottom), totaling an internal volume of 20.6 mm^3.

Prior studies have shown that the primary driver of the actuator's frequency is the internal volume of this cavity, and with a small internal volume, the actuator will pulse at very high frequencies [7]. The operating conditions of h/d = 1.8 and NPR = 4.9 were fixed for the experiments conducted in this study wherein the actuator's core flow jet pulses at approximately 19 kHz. As previously stated, the co-axial flow is not enabled for this series of experiments, though the companion paper by Solomon, et al. [8] at Tuskegee University explores an activated co-axial flow for spectral and velocity field measurements.

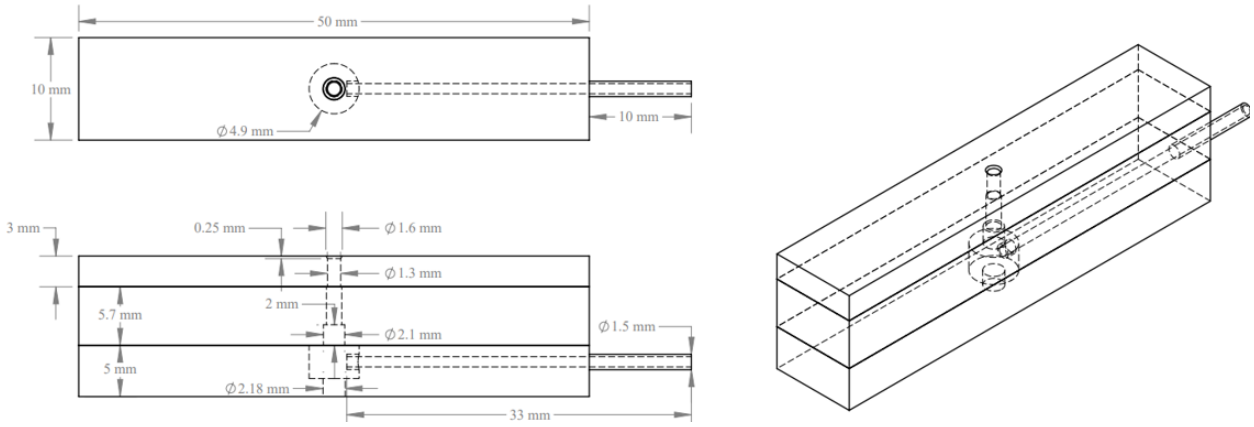

Fig. 2 Detailed CAD drawings of the Tuskegee University co-axial injector.

B. Focused Laser Differential Interferometry (FLDI)

The FLDI configuration, illustrated in Fig. 3, begins with a 10 mW He-Ne laser with a wavelength of 633 nm which first passes through an F = -9 mm expansion lens. Next, the beam's polarization is rotated 45° by a polarizer, such that the beam splits into two equal pairs when passing through a subsequent Wollaston prism. A focusing lens then brings the beam pairs to a focal point which is carefully aligned with the actuator's core flow jet centerline. At the focal point, the beams have diameters (represented by r) of 26.4 μm and a spacing of Δx = 97 μm, as measured by a beam profiler (Fig. 4). Beyond the focal point, which is the FLDI probe location, the beams re-expand to the catch side of the apparatus. An inverted optical arrangement recombines the beams before they pass through an expansion lens (of a different focal length [F = -50 mm]) and refocus onto a photodetector. On the photodetector, the beams create an interference pattern that changes in proportion to the density fluctuations that occur at the beams' foci in the test section. The photodetector's output voltage is monitored at high sampling rates (1.25 MHz) with a National Instruments USB-based data acquisition (DAQ) system (Model USB-6356).

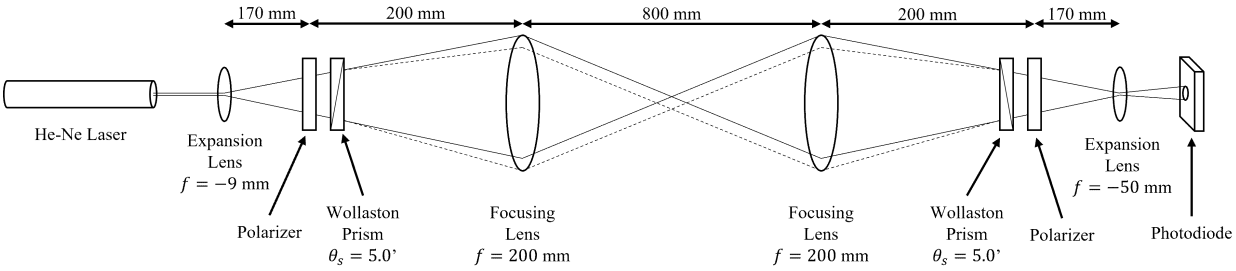

Fig. 3 Schematic of standard FLDI set up including optics dimensions and spacing.

The spectral content of the disturbances measured by FLDI can be computed directly from the photodetector signal. Comparisons are made between the FLDI spectral content and the acoustic spectra from a microphone; this is important as the FLDI measurement probes the flowfield while the microphone measures the acoustic emission in the near-field. The signals from both the photodetector and microphone are simultaneously sampled through a LabVIEW program interfacing with the DAQ module. Additional details on this experimental arrangement are provided in Section II.E.

Downloaded by John Solomon on July 15, 2023 | http://arc.aiaa.org | DOI: 10.2514/6.2023-4240

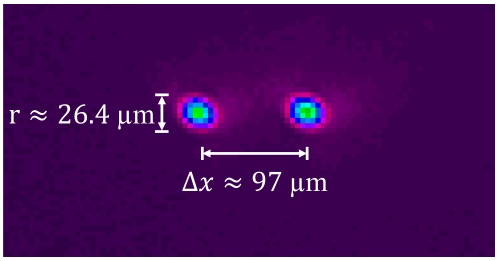

Fig. 4 Beam profiler image displaying FLDI ray size and spacing at the focal point.

Gragston, et al. [9] recently developed an FLDI configuration known as linear array FLDI (LA-FLDI) that creates an $m \times n$ array of beam pairs in a single configuration. This new configuration creates multiple beam pairs with the addition of a diffractive optical element (DOE) between the first expansion lens and Wollaston prism. LA-FLDI allows simultaneous measurements at numerous locations in the flow depending on the parameters of the DOE. The number of beam pairs must match the number of photodiodes used to collect the signals. With several measurement locations placed within the flowfield, cross-correlations can be computed to measure the convective velocity of turbulent structures present within the flow by determining the lag time between the signals of different beam pairs. With precise measurements of the LA-FLDI beam pair positions and the cross-correlation lag times, one can estimate the convective velocities of turbulent structures.

In this study, a 1×6 array is created and positioned along the core flow jet centerline with the points aligned in the streamwise direction. The furthest upstream point of the array (and the singular point for the FLDI measurements) is placed approximately 1 mm from from the jet exit plane. The beam pairs in the LA-FLDI array are spaced 2060 μm apart, spanning a total distance of 10.3 mm from the first to the sixth beam. In the LA-FLDI measurements, each of the beam pairs in the array have beam diameters of 26.1 μm and a spacing of 102 μm (recall that each point in the array is comprised of a pair of beams with finer spacing). In the current configuration, the 6 beam pairs allow for the calculation of 5 convective velocities. To achieve higher resolution in the convective velocity measurements, the actuator assembly (the source jet and co-axial injector) were fixed to a motorized translation stage that was moved in 0.5 mm increments. The LA-FLDI experiments were conducted for a total of 35 streamwise locations that spanned 17.5 mm across each beam pair and a total of 26 mm between the first and last beam pair.

C. Schlieren Imaging for Flow Visualization

A small-scale, lens-based schlieren system installed on the optical benchtop is used to visualize the actuator's flowfield. High-speed images are collected with a Photron FASTCAM SA-Z at 200 kHz, or 200,000 frames per second. In this manner, the actuator's high-frequency resonance is measured with sufficient temporal resolution to view approximately 10 images per cycle. A high-powered, pulsed LED light source that was assembled in-house provides illumination with a 1 μs pulse width which is long enough to adequately expose the image and short enough to freeze the high-speed flow structures. The LED illumination is focused onto a narrow iris to provide a point-source of light to the first schlieren lens which is a 2" diameter, F = 300 mm plano-convex lenses. The second lens (with the same specifications) is placed beyond the actuator assembly, and it focuses the light to a point where a knife-edge cuts off approximately 50% of the light. The knife-edge orientation is chosen such that the schlieren images are sensitive to gradients in the spanwise direction across the jet produced by the actuator (i.e., the knife-edge is parallel to the jet centerline). A Sigma 70-200 mm lens provides high-magnification of the schlieren test area to the camera's sensor.

D. Particle Image Velocimetry (PIV)

Planar particle image velocimetry (PIV, or 2D-PIV) have been conducted to provide direct measurements of the actuator velocity fields. In this arrangement, two-component velocity fields are measured for a few different configurations. The first configuration is focused on measuring the velocities of the actuator's 1.5-mm-diameter source jet. This case serves to validate the PIV measurements at these small scales and high velocities. Additional cases included the actuator operating in a steady manner (by setting h/d to 0) and the actuator operating in resonance, or in its pulsed mode of operation. For the steady actuator output, the source jet pressure is fixed at NPR = 4.9 (i.e., the same pressure required for the pulsed operation) while the impingement distance is zeroed ($h/d = 0$) to force steady flow

Downloaded by John Solomon on July 15, 2023 | http://arc.aiaa.org | DOI: 10.2514/6.2023-4240

behavior. In the pulsed mode of operation, h/d is set to 1.8, where the actuator pulses at approximately 19 kHz. In each of these measurements, the laser sheet thickness is minimized, and the sheet is carefully aligned with the jet's and actuator's centerline. Figure 5 shows a photograph of the experimental setup for the PIV measurements. Additional details covering the PIV measurements are provided in the subsequent paragraphs.

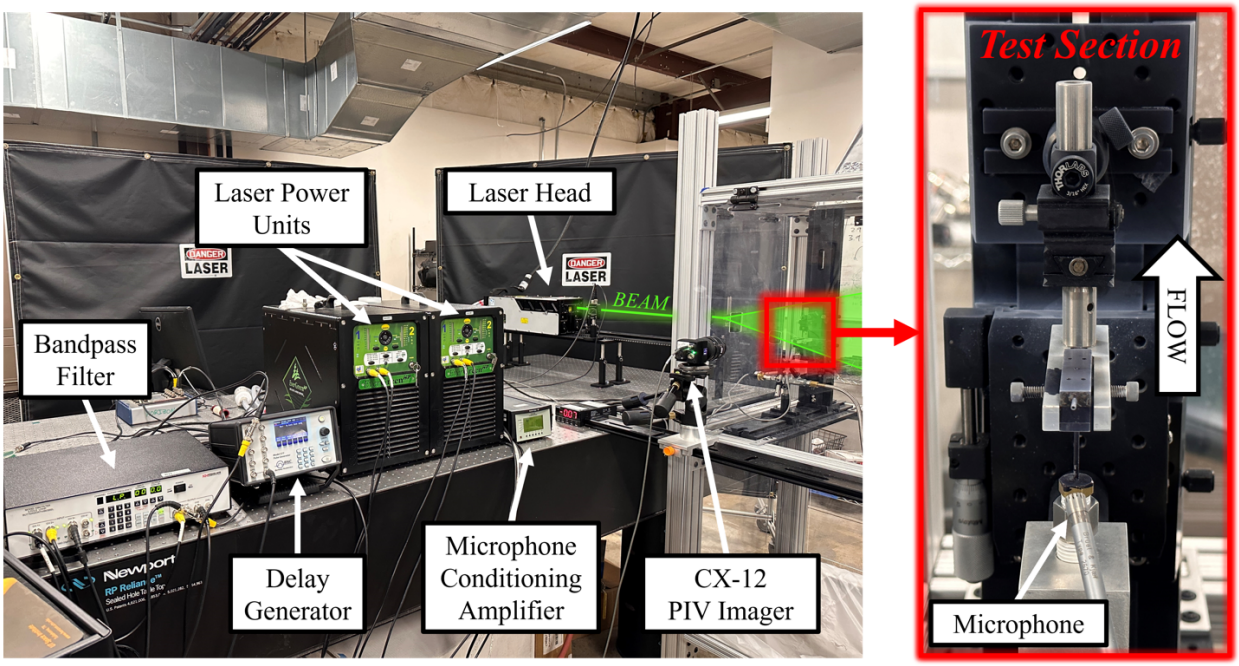

Fig. 5 Photograph of the experimental setup for the PIV measurements.

Laser illumination is provided by a Quantel Evergreen EHP30 double-pulsed Nd:YAG laser. For the present study, the repetition rate is set to a nominal value of 30 Hz while the average power output is tuned and measured to be 21 mJ/pulse. The sheet-forming optics used in these experiments are a $F = 300$ mm plano-convex spherical focusing lens followed by a $F = -9.7$ mm plano-concave cylindrical expansion lens. These optics are placed such that the sheet waist is coaxial with the flow being measured. The beam waist is measured to be no more than 0.7 mm. The pulse separation for acquiring the image-pairs is fixed at $\Delta t = 1\mu s$ for each case in the present study. A photodiode placed near the laser output is used to verify the timing of the laser with the camera exposure and the microphone.

The flow is seeded with titanium dioxide (TiO_2) particles that are atomized in a fluidized-bed seeder. The particles have a reported nominal diameter of 21 nm [10, 11]. As TiO_2 can be absorbent and the particles must travel through small flow areas, the seed particles were baked in a laboratory oven to reduce moisture and prevent particle agglomeration. The fluidized-bed seeder, which was constructed in-house, is supplied compressed nitrogen from a pressurized cylinder. A series of regulators and valves controls the flow and maintains the pressure within the seeder. The pressurized nitrogen with suspended TiO_2 particles is then plumbed to the source jet to seed the actuator flowfield.

Images are acquired using a LaVision Imager CX-12 camera with a 12 MP sensor and a 12-bit digital output. A Nikon 50 mm f/1.4 lens is paired with the camera to image the region of interest with sufficient magnification and resolution: the images are masked to a region encompassing 1751 px by 639 px which corresponds to a resolution of 43.38 mm by 15.83 mm. Image sets are recorded at a nominal rate of 30 Hz, with some variation in the acquisition rate stemming from the phase-locked acquisition process when the actuator was pulsing. Further details on the phase-locked triggering configuration are provided in Section II.E. Five hundred (500) image pairs are acquired for each recording to ensure convergence of the averaged velocity fields.

The vector fields are computed from all image pairs using LaVision's commercial software package, DaVis version 10.2. In each image set, the image pre-processing routine used in this experiment includes background subtraction and pixel multiplication to improve the contrast of illuminated seed particulates. A multipass cross-correlation algorithm is used for vector calculations. Four initial passes are conducted with an interrogation window that is elliptically weighted 4:1 in the streamwise direction and set to a nominal size of 96 px $\times$ 96 px. An overlap of 50% is used in the initial passes.

Downloaded by John Solomon on July 15, 2023 | http://arc.aiaa.org | DOI: 10.2514/6.2023-4240

The final interrogation window is set to an adaptively shaped 32 px × 32 px region, and eight passes are used with 75% overlap. Postprocessing of the calculated vector fields involves the application of the universal outlier detection scheme with five passes of a 7 by 7 vector region to remove erroneous vectors. The PIV vector fields computed by DaVis for these parameters have a vector resolution of 220 by 82 for the region of interest.

Uncertainties in velocity measurements from PIV depend on several different factors [12]. The challenges associated with the present experimental configuration include the small physical and temporal scales associated with the actuator and the large dynamic range of velocities present within the jet flowfield. To quantify the uncertainties in these data, an *a posteriori* method using correlation statistics, as outlined by Wieneke [13], is explored. The uncertainties are computed within DaVis, and the uncertainty fields are inspected for each case reported in this paper. The uncertainty fields are shown for the steady actuator output as well as two phases from the actuator's pulsed operation. These uncertainties are representative of the typical uncertainties that have been computed across all cases.

E. Data Acquisition and Processing Methodology

The experiments presented in this paper have been performed on an optical benchtop in UTSI's Tennessee Aerothermodynamics Laboratory (TALon). During the FLDI and PIV experiments, a Brüel & Kjær microphone (Type 2670) is placed approximately 50 mm from the source jet impingement location to sample the acoustic emission resulting from the resonance created by the actuator. The microphone signal is used to validate the spectral content computed from the FLDI signals and to phase-lock the PIV image acquisition during the pulsed actuator cases. During the FLDI experiments, a National Instruments Model USB-6356 data acquisition system simultaneously monitors the outputs of the photodetector and microphone at a sampling rate of 1.25 MHz. In the LA-FLDI experiments, the same DAQ system simultaneously samples the outputs of all six photodetectors at a rate of 1.25 MHz in addition to the microphone's signal. For the PIV experiments, the DAQ system collects data from the microphone and the laser-monitoring photodiode at a sampling rate of 1 MHz.

In each experiment, the microphone is connected to a Brüel & Kjær Nexus 2690 conditioning amplifier whose output is monitored by the data acquisition platform in LabVIEW. In the phase-locked PIV experiments, the microphone signal is low-pass filtered at 40 kHz through a Krohn-Hite Model 3384 filter to ensure that the actuator's spectral content does not contain aliased frequencies. The microphone signal is also bandpass filtered with frequencies passed between 15 kHz and 21 kHz to isolate the actuator's resonance peak for phase-locking. The output of the bandpass filter is amplified by 10 dB to ensure proper triggering occurs. A block diagram shown in Fig. 6 illustrates the components involved in the phase-locked measurements. The bandpass filtered signal is provided as a trigger input to a BNC Model 577 pulse generator to produce TTL-style trigger signals to LaVision's Programmable Timing Unit (PTU X). The pulse generator is set to operate with an external trigger that detects rising edges in the bandpass microphone signal. Because the Evergreen EHP30 laser used for the PIV experiments operates at a nominal repetition rate of 30 Hz, the pulse generator's output is inhibited for $f_{act}/30$ Hz trigger events (where f_{act} is the actuator resonance frequency) such that the phase-locked trigger output signal did not exceed 30 Hz. This signal is provided to the LaVision PTU which initializes the laser and camera.

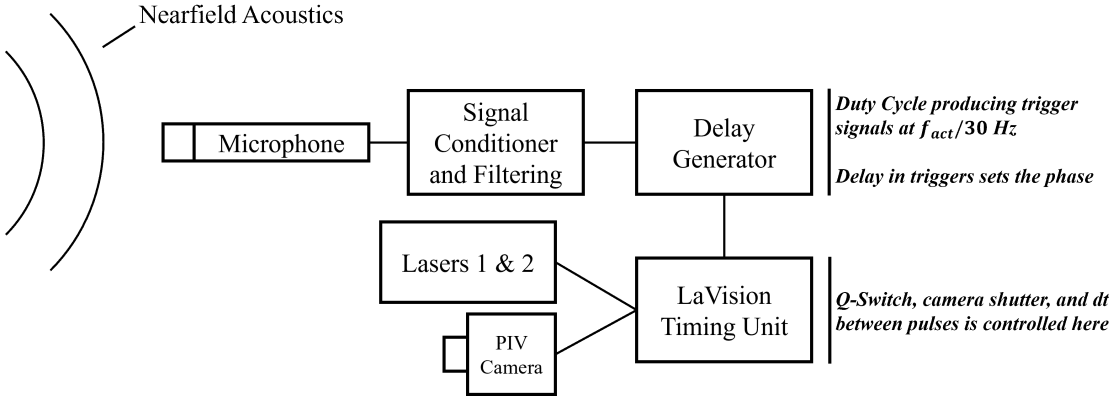

Fig. 6 Block diagram illustrating the phase-locked acquisition process for the PIV experiments.

Downloaded by John Solomon on July 15, 2023 | http://arc.aiaa.org | DOI: 10.2514/6.2023-4240

With this type of fluidic actuator, there can be some jitter [4] in the resonant frequency due to the nature of fluidic / acoustic resonance that this device relies upon for its pulsed operation. As a result of this jitter, the phase at which a trigger signal is generated may not precisely line up with a constant phase at which the PIV images are collected. This is caused by the trigger initiating the laser illumination which typically takes 135 μs (the Q-switch delay) to output at full power. Over this period of time, the actuator completes two cycles and is approximately 60% through with a third (see Eq. 1). As such, the jet structure and velocity fields may vary slightly from image to image. Several of the trigger events and photodiode peaks were compared to ensure that the effects from jitter are minimized. Further, the 500 image-pairs acquired for each phase provide a sufficient number of samples to properly converge the phase-averaged velocity fields.

$$19.1 \text{ kHz} \times 135\ \mu\text{s} \approx 2.6 \text{ cycles} \tag{1}$$

III. Results and Discussions

Flow visualizations from the lens-based schlieren experiments can be seen in Fig. 7 which shows a collection of typical instantaneous images extracted from one cycle of the actuator operating in a pulsed manner. In the image sets, a horizontal knife edge was used allowing density gradients in the spanwise direction to be visualized. From this orientation, both the shock structures as well as the shear layer are clearly visualized. In the first image ($\phi = 0°$), the formation of a compressible vortex is seen as the actuator's core flow jet begins emitting from the nozzle. This vortex forms at the orifice from the rising pressure within the actuator's impingement cavity. During the following phases up to $180° < \phi < 240°$, the shock structures trailing the vortex / jet front indicate a supersonic, high momentum microjet ejection process. At $\phi = 240°$, a buildup in pressure within the cavity creates spillage from the actuator at the source jet impingement location (not imaged here). This process, which has been mentioned previously [4], causes the pressure in the actuator to decrease which subsequently reduces the jet exit velocity. At this point in the cycle, the compressible vortex has broken down into smaller turbulent structures and has begun mixing with the ambient air. Lastly, at $\phi = 300°$ the bulk of the ejected fluid has convected downstream while another compressible vortex can be seen forming near the nozzle exit. This indicates that the actuator cavity is beginning to pressurize and that another cycle is beginning.

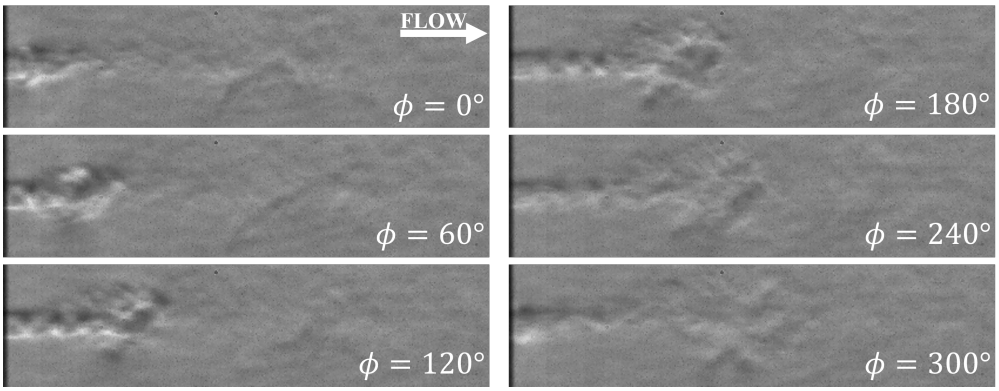

Fig. 7 Instantaneous high-speed schlieren images extracted from one typical cycle.

Figure 8 shows a comparison of the acoustic spectra calculated from the B&K microphone and the power spectral density (PSD) computed from the FLDI measurement. The microphone, placed 50 mm from the source jet impingement location, can be seen to have a 19.16 kHz tone. At higher frequencies, the low-pass filter's rolloff (cutoff set to 40 kHz) can be seen to remove unwanted tones. The tone indicates strong resonance of the actuator around the design frequency, as predicted. The FLDI PSD shows excellent agreement in the spectral content, with a dominant peak located at 19.23 kHz. A similar methodology has been reported by Price, et al. [6] for measuring acoustic emission resulting from jet screech. FLDI has proven to be a strong diagnostic tool for characterizing ultra-high frequencies in small scale domains due to its high sensitivity to density gradients and no need for signal filtering.

As previously stated, this study focuses solely on the dynamics and velocity field measurements of the actuator's central core flow jet. All velocity field measurements are conducted at an NPR of 4.9. Initial PIV experiments were conducted on the source jet alone to verify the accuracy of the measurements. Subsequent PIV experiments were focused on the actuator's jet operating in a steady mode (with $h/d = 0$) and in a pulsed mode that produces the 19 kHz

Downloaded by John Solomon on July 15, 2023 | http://arc.aiaa.org | DOI: 10.2514/6.2023-4240

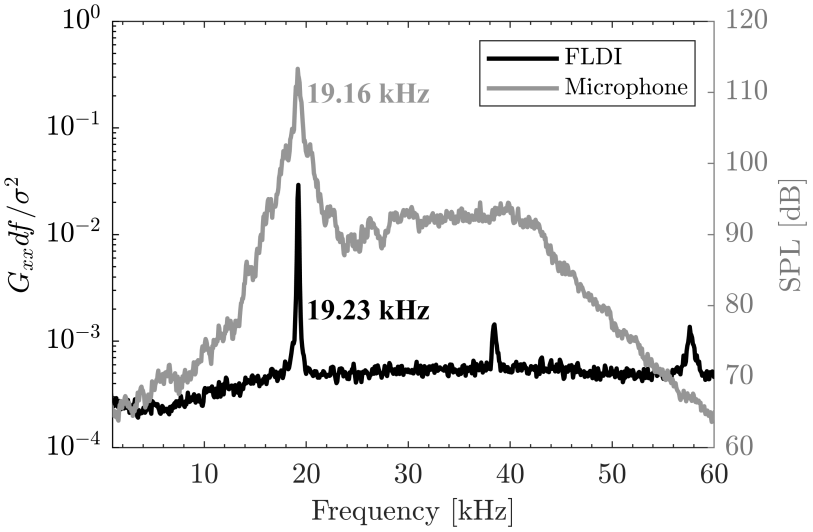

Fig. 8 Spectral content computed from the FLDI and microphone signals.

Downloaded by John Solomon on July 15, 2023 | http://arc.aiaa.org | DOI: 10.2514/6.2023-4240

tone (with $h/d = 1.8$). The first measurements presented here are for the steady flow emanating from the source jet. In this case, the actuator assembly is removed, and the source jet emanates into the ambient. The source jet pressure was set to NPR = 4.9 to mimic the flow conditions required for pulsed operation of the co-axial injector. Under these conditions, the source jet produces an underexpanded flow at a fully-expanded Mach number of $M_s = 1.7$ as calculated from Eq. (2). Here, γ is the ratio of specific heats ($\gamma = 1.4$ for air), p_0 is the stagnation pressure supplied to the jet nozzle (which is a straight tube), and p_a is the ambient pressure.

$$M_s = \left(\frac{2}{\gamma - 1}\right)^{\frac{1}{2}} \left[\left(\frac{p_0}{p_a}\right)^{\frac{\gamma-1}{\gamma}} - 1\right]^{\frac{1}{2}} \tag{2}$$

The steady source jet's ensemble-averaged streamwise velocity field (u) is shown in Fig. 9. Here, the spanwise (y) and streamwise (x) coordinates are non-dimensionalized by the source jet diameter ($d_s = 1.5$ mm). It is clear that the jet is underexpanded since the flow exits at nearly 350 m/s before accelerating downstream to nearly 450 m/s. Furthermore, the flow remains supersonic for an extent spanning approximately twelve jet-diameters downstream (i.e., to $x/d \approx 12$). With the small scales associated with this flowfield limiting the vector resolution, it is difficult to discern the shock cells and Mach disk that occur within the flow structure of this underexpanded jet. Regardless, the velocities measured within the jet core are clearly supersonic, and the jet structure is qualitatively similar to that reported in Kreth, et al. [4], albeit with less resolution in the present case as a consequence of the larger region of interest. The uncertainty field for this case was inspected but is not shown here, as these values are presented for the steady and pulsed actuator cases which have higher uncertainties.

Following the PIV experiments on the steady source jet, the actuator's flowfield was studied when it is operated in a steady manner. To prevent the actuator from resonating, the source jet was moved such that no space was between its exit and the actuator's entrance, or such that $h/d = 0$. The same pressure was supplied to the source jet such that NPR = 4.9 was maintained across each configuration. The ensemble-averaged streamwise velocity field for the steady actuator jet is shown in Fig. 10. It is important to note that the spatial coordinates for this case have been normalized by the actuator's jet diameter which is now $d_m = 1.0$ mm (instead of $d_s = 1.5$ mm from the Fig. 9). With this non-dimensionalization, direct comparisons can be made between the two cases. Interestingly, the steady jet emitting from the actuator appears to be subsonic, even at the exit. The calculated velocities do show that the flow accelerates downstream and reaches a global maxima of approximately 300 m/s at $x/d \approx 10$ along the centerline. To investigate these results further, the uncertainties in the ensemble-averaged streamwise velocity are shown in Fig. 11.

As mentioned in Section II.D, the uncertainties are computed within DaVis 10.2 using the correlation statistics method outlined by Wieneke [13]. The uncertainty values shown in Fig. 11 have been normalized by the global maxima of the streamwise velocity observed in the ensemble-averaged vector field from Fig. 10. As expected, much of the

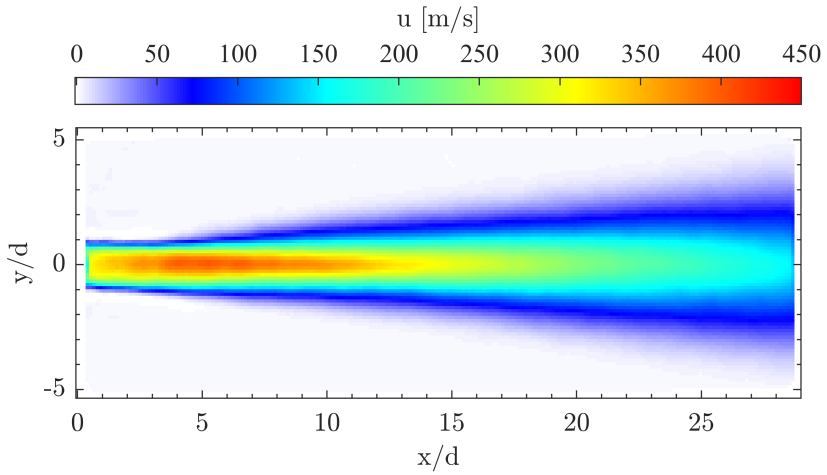

Fig. 9 Ensemble-averaged streamwise velocity field for the source jet at NPR = 4.9.

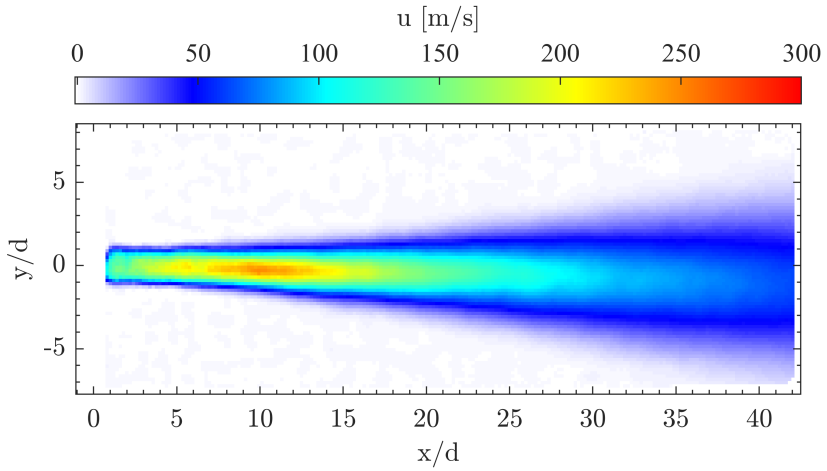

Fig. 10 Ensemble-averaged streamwise velocity field of the actuator's core flow jet in a steady mode of operation with NPR = 4.9 and $h/d = 0$.

uncertainty is concentrated around the jet exit location where the velocities are expected to be the largest and where new seed particles are introduced into the field of view. In the jet core, the uncertainties reach levels of 4-6% for $0 < x/d < 7$, but the uncertainties rapidly diminish to approximately 1-2% by $x/d > 12$. While the reported uncertainties are sufficiently low for this case, it is apparent that there may be bias errors present when the actuator is installed. It is reasonable to expect that the conditions used in the steady actuator operation should result in sonic exit conditions with potential for the flow to be mildly underexpanded. As the internal geometry seen by the flow is quite complex with narrow flow areas, the authors suspect that the geometry may cause the seed particles to have some lag in their ability to follow the flow. Further study is needed to uncover additional sources of uncertainty and to eliminate others.

In addition to inspecting the uncertainty fields for the ensemble-averaged streamwise velocity component, the convergence of the ensemble-average was inspected at several locations within the field of view. Figure 12 shows the convergence in the streamwise velocity at a location along the jet centerline where the local flow velocity is a maximum ($u \approx 250$ m/s at $x/d \approx 10$). At this location, a running estimate of the ensemble-averaged velocity is computed (as $\bar{\tilde{U}}$). The final computed value of the ensemble-average is subtracted from the running estimate, and that quantity is normalized by the final value [12]. This value is plotted as the black line in Fig. 12, and the dotted lines bounding

Downloaded by John Solomon on July 15, 2023 | http://arc.aiaa.org | DOI: 10.2514/6.2023-4240

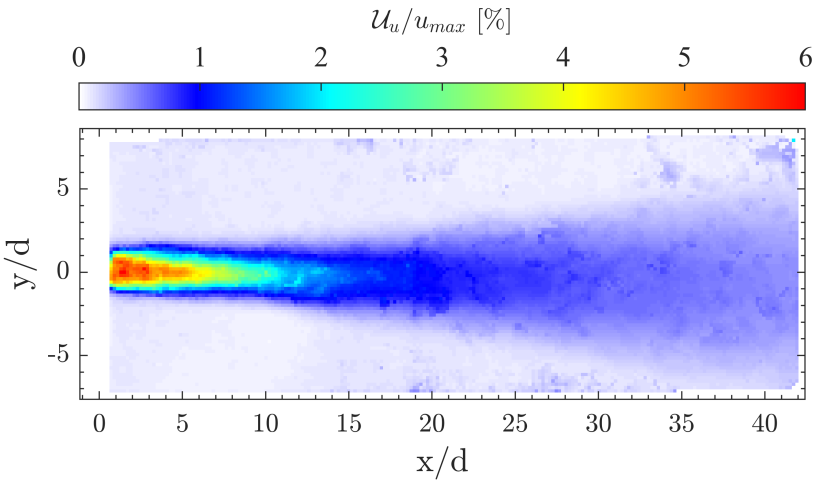

Fig. 11 Uncertainty in the ensemble-averaged streamwise velocity field of the actuator's core flow jet in a steady mode of operation with NPR = 4.9 and $h/d = 0$.

this curve corresponds to the 95% reliability interval for the running average. It is important to note that the bounds on this graph correspond to 20% deviation and that the curve converges to within 1.5% of the final value by image 300. Several additional locations within the field of view were probed in a similar manner to ensure that the mean streamwise velocity had converged, but only the location of the maxima is shown here. These additional locations were chosen based on regions where the turbulent kinetic energy was maximized (i.e., along the centerline and for $x/d < 5$) and where the velocity gradients were the strongest (e.g., in the shear layer). In most regions, the convergence of the ensemble-averaged streamwise velocity component occurs more quickly than that shown in Fig. 12.

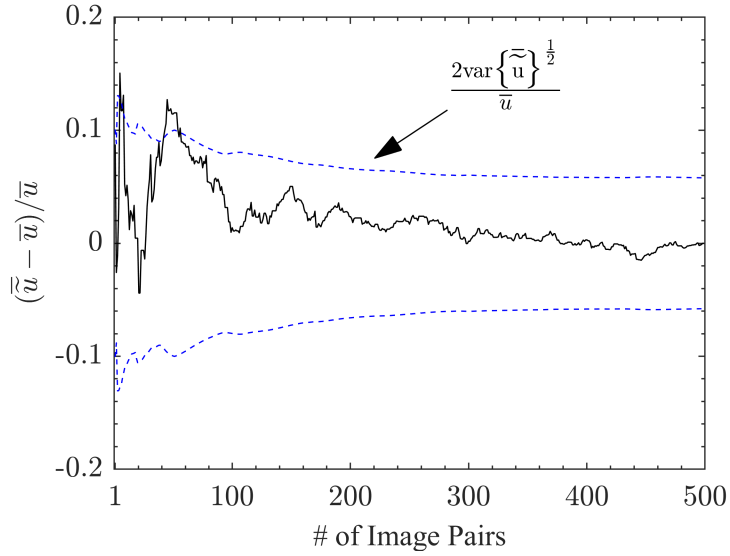

Fig. 12 Typical convergence of the ensemble-averaged streamwise velocity component for the actuator's output for the steady mode of operation.

Following the velocity field measurements for the steady actuation jet, phase-locked PIV measurements were conducted with the actuator pulsing at 19.1 kHz with $h/d = 1.8$ and NPR = 4.9. Five hundred image-pairs were collected for each phase, and the resulting velocity fields were phase-averaged. The phase-averaged streamwise velocity

Downloaded by John Solomon on July 15, 2023 | http://arc.aiaa.org | DOI: 10.2514/6.2023-4240

fields for six phase increments ($\Delta\phi = 60°$) are shown in Fig. 13. As with the steady actuation case, the PIV field of view encompasses 15 jet-diameters in the spanwise direction (y/d) and 42 jet-diameters in the streamwise direction (x/d), where d references the actuator exit jet diameter, $d_m = 1.0$ mm. Variations in the streamwise velocity fields across the cycle are most apparent within the jet core ($x/d \approx 5$) where the local velocities range from $\bar{u} \approx$ 180-200 m/s at $\phi = 0°$ and 300° to $\bar{u} \approx$ 240-250 m/s at $\phi = 180°$. As the cycle begins at $\phi = 0°$, the pulsed jet flow accelerates until $\phi = 180°$ where the streamwise velocities are maximized. In the subsequent phases ($\phi = 240°$ and 300°), the flow decelerates as the cycle finishes and repeats. Interestingly the flow structure downstream for $x/d > 10$ does not show much variation across the different phases; however, this can be attributed to the reduced local velocities as the jet spreads and the structures convect downstream. As this occurs, the actuator continues to pulse at approximately 19.1 kHz where one cycle spans only $T_P = 52.2\mu s$. With this high-frequency oscillation occurring at the jet exit, the slower flow regions only move slightly downstream, especially when imaged only 60° apart ($T_P/6 = 8.7\ \mu s$). Over this amount of time, a packet of fluid moving at 100 m/s will only displace by 0.87 mm which corresponds to $\Delta x/d = 0.87$. It is also important to note that the velocities measured here are all subsonic, where some regions of supersonic flow were expected based on the flow visualizations conducted with high-speed schlieren imaging. The authors believe that similar bias errors may be present in these cases, requiring further study.

Downloaded by John Solomon on July 15, 2023 | http://arc.aiaa.org | DOI: 10.2514/6.2023-4240

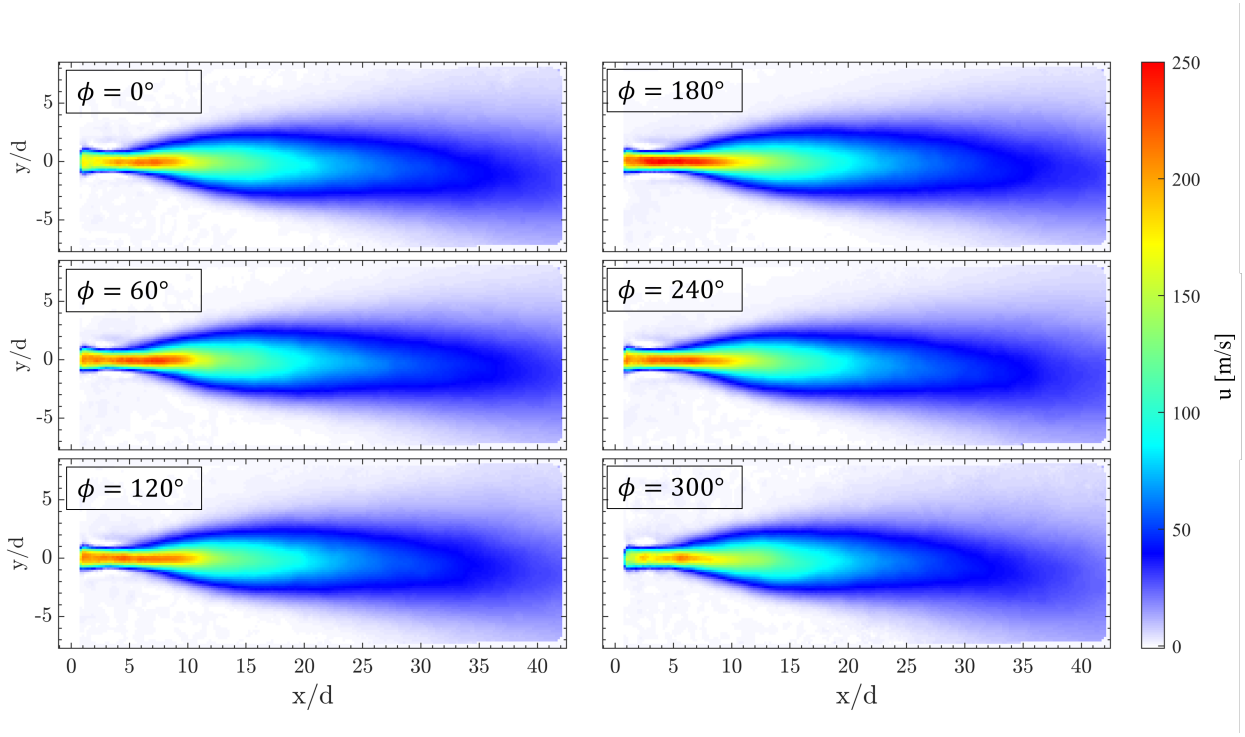

Fig. 13 Phase-averaged streamwise velocity fields measured at six phase increments of $\Delta\phi = 60°$ with NPR = 4.9 and $h/d = 1.8$.

As with the steady actuation case, the uncertainties in the phase-averaged streamwise velocity fields have been computed and inspected. The uncertainty fields for the beginning and mid-cycle phases of $\phi = 0°$ and 180° are shown in Fig. 14. As before, these values are non-dimensionalized by the maximum streamwise velocity observed in each respective case, and the regions with the largest uncertainties are concentrated near the jet exit location. In the phase-locked PIV measurements, the uncertainties only reach 4-4.5% for $0 < x/d < 5$ for $\phi = 0°$ (the beginning of the cycle) and only 2-3% for the same region for $\phi = 180°$ (the portion of the cycle with the highest velocities). The uncertainties rapidly diminish outside of the jet core for all phases, as expected.

Figure 15 shows the convergence of the phase-averaged streamwise velocity component for the same two phases of $\phi = 0°$ and 180°. The methodology to compute the uncertainties and in plotting them are the same as in the steady actuation case. Here, the same probe location was chosen for each phase (at the maximum velocity location for $\phi = 180°$), and the values shown here are representative of the typical convergence seen across regions with high

Downloaded by John Solomon on July 15, 2023 | http://arc.aiaa.org | DOI: 10.2514/6.2023-4240

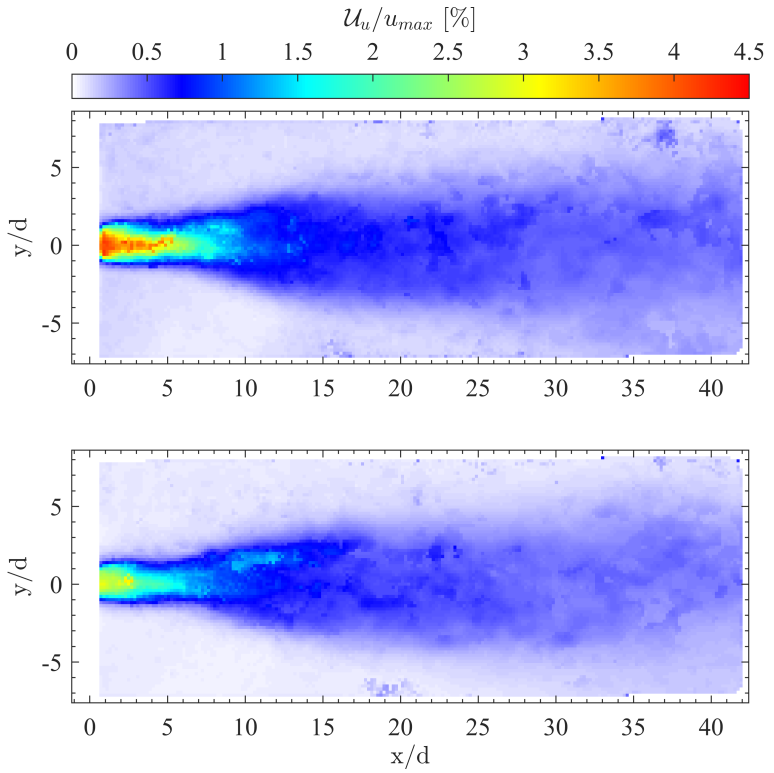

Fig. 14 Uncertainty of the phase-averaged streamwise velocity of the actuator's output at phases $\phi = 0°$ (upper) and $180°$ (lower).

turbulent kinetic energy and with large spatial velocity gradients. However, most of the locations chosen within the field of view converge more rapidly as the velocity fluctuations outside of the core flow region are not as large as those shown here.

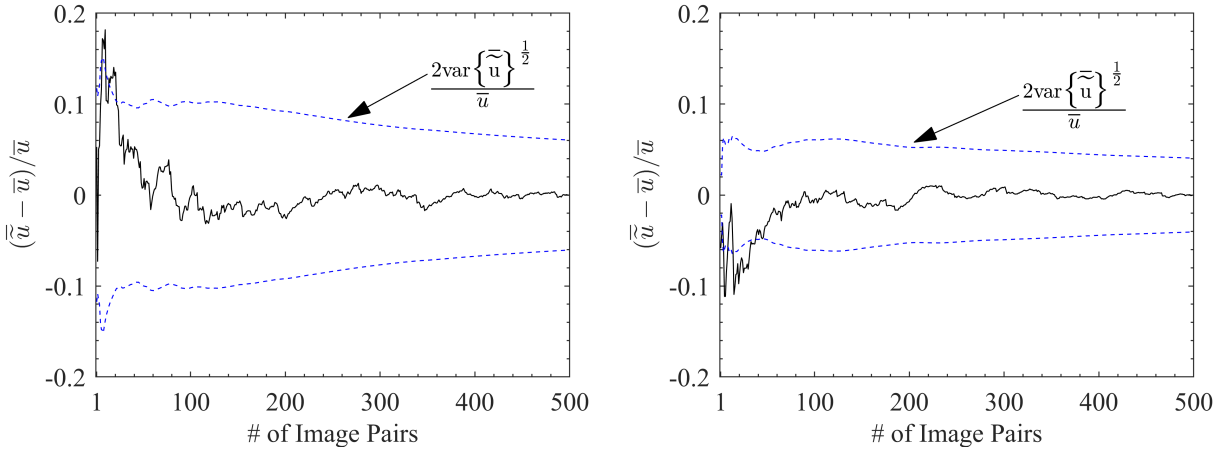

Fig. 15 Convergence of the phase-averaged streamwise velocity components at phases $\phi = 0°$ (left) and $180°$ (right).

Having computed the phase-averaged velocities for six phases, a cycle-averaged velocity contour can be obtained to illustrate the average flow velocities expected in pulsed operation. The cycle-averaged velocity field is shown in Fig. 16. In comparing these data with those from the steady mode of operation, stark differences in the overall flow structure are

clearly observed. Although the cycle-averaged velocity shows a maximum of approximately 240-250 m/s, the structure downstream of $x/d \approx 10$ shows significant spreading of the pulsed jet compared to the steady actuation jet. For the steady case (recall Fig. 10), the streamwise velocity reached a maximum of approximately 280-300 m/s at $x/d \approx 10$, though the jet spreads significantly slower. From the cycle-averaged velocities, it is clear that the pulsed actuation can enable more substantial mixing over short distances from the actuator.

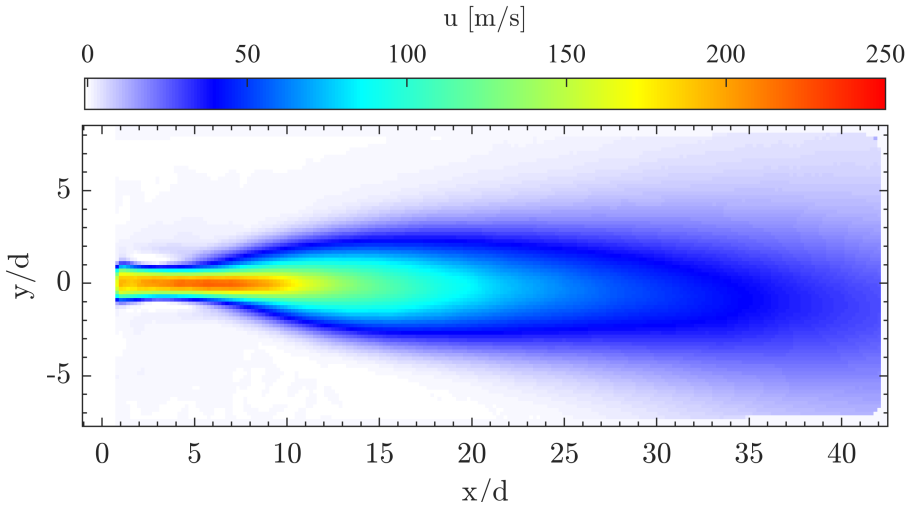

Fig. 16 Cycle-averaged (across all six phases) streamwise velocity field for the actuator's pulsed operation with NPR = 4.9 and $h/d = 1.8$.

Using the phase-averaged and cycle-averaged velocity fields, centerline velocity profiles were extracted and compared to the convective velocity measurements obtained from cross-correlations of the LA-FLDI measurements. These results are presented in Fig. 17. Here, the two phase-averaged centerline velocity profiles were extracted for $\phi = 0°$ (red) and $\phi = 180°$ (blue), where the lowest and highest velocities are seen, respectively. The centerline velocities from the phase-averaged case were also extracted and are shown (black). The convective velocities computed from the LA-FLDI cross-correlations are shown as hollow circles. These values were measured across several different measurement locations with a motorized translation stage traversing the extent shown.

All centerline velocity profiles show an initial acceleration, but the peak locations differ slightly. From $0 < x/d < 4$, the LA-FLDI and $\phi = 180°$ velocities are in excellent agreement, with a peak velocity of 250 m/s reached at $x/d \approx 4$. For the $\phi = 0°$ and cycle-averaged cases, the velocity reaches its maximum value further downstream, and both are nearly 220 m/s. After the jet core, each of the velocities measured in the PIV experiments show similar decay rates, and each converge by $x/d \approx 20$. After the jet core, the convective velocities measured from the LA-FLDI experiments show a more rapid deceleration, but by $x/d \approx 20$, the values also converge with the other cases. As these measurements involve separate experimental configurations, the differences could be attributed to random experimental variations introduced from the different setups. Because of the high sampling frequency used in the LA-FLDI measurements (1.25 MHz), estimates of the convective velocity were expected to represent those in a cycle average sense. This could warrant further investigation as to why the LA-FLDI convective velocities show a higher peak velocity than the PIV cycle average. The authors hypothesize that this could be due to the LA-FLDI system being more sensitive to the density gradients that will occur for the faster velocities in the 180° phase, leading to more agreement with the data from that phase in the PIV measurements. Some additional insight should be sought with further investigation of these results.

IV. Summary and Future Work

An experimental investigation focused on characterizing the flow emanating from a high-frequency, pulsed co-axial injector has been conducted using a series of optical diagnostics. The actuator was developed at Tuskegee University and is designed to produce a high-frequency, pulsed, supersonic jet that interacts with a co-flow annular stream to enhance mixing of the two streams. The actuator used in the present study produces a jet that pulses at a frequency of 19.1 kHz, or an alternate arrangement can make the jet steady. In these experiments, only the core flow jet was used (i.e.,

Downloaded by John Solomon on July 15, 2023 | http://arc.aiaa.org | DOI: 10.2514/6.2023-4240

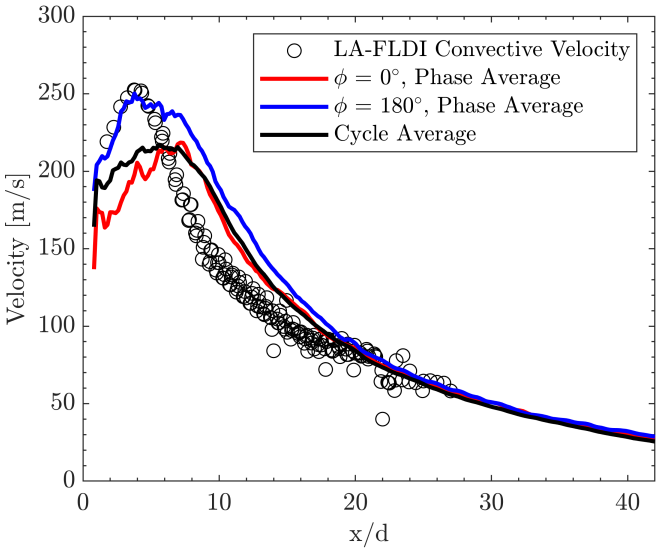

Fig. 17 Centerline velocity profiles extracted from the various experimental techniques. Convective velocities computed from the LA-FLDI measurements are compared with the PIV measurements from phases $\phi = 0°$ and $180°$ as well as the cycle-averaged velocities.

there is no co-flow), and both the steady and pulsed modes of operation were explored. Measurements were conducted with high-speed schlieren imaging, focused laser differential interferometry (FLDI), and phase-locked particle image velocimetry (PIV). Additionally, the actuator's resonance was monitored with a microphone placed in the near-field. With these diagnostics, the flowfield has been visualized, the spectral content has been characterized, and the velocity fields have been measured.

Direct velocity measurements were conducted with planar PIV for the actuator's steady source jet and for the actuator's steady core flow jet. The PIV system was then phase-locked with the microphone signal providing the trigger such that the pulsed jet could be measured at various phases. Results were compiled for six different phases, and the phase-averaged velocity fields indicate that the actuator's pulsed jet produces significant flow velocities that can enhance mixing if the co-flow is enabled. The phase-averaged velocities of the pulsed jet were expected to be supersonic for some portions of the cycle, though the results obtained in this study show that these velocities did not exceed 250 m/s. The ensemble-averaged velocities obtained from the steady source jet did show the expected behavior of an underexpanded jet, indicating that any experimental errors may have resulted from the actuator.

While these results warrant further investigation, good agreement was observed when comparing the centerline velocities measured from phase-locked PIV with convective velocities obtained through cross-correlation analyses of the FLDI measurements. Using the new linear array FLDI (LA-FLDI) technique developed in-house at UTSI, several measurement locations within the flow can be probed simultaneously. The resulting signals can be cross-correlated to obtain estimates of the convective velocity of turbulent structures or disturbances that propagate through the measurement region. The LA-FLDI convective velocity measurements show excellent agreement with the phase-averaged centerline velocities obtained from the pulsed jet phase with the maximum velocities. In addition to the agreement observed with these measurements, the calculated uncertainties in the PIV vector fields show that the overall uncertainties are relatively low compared to the velocities measured (less than 5-6%).

Future work should focus on uncovering any additional sources of uncertainty and on eliminating / minimizing any sources that can be controlled. Further investigation of the actuator at different operating conditions is also warranted to see if the flow structure is similar across the various phases. Follow-on efforts should additionally focus on characterizing the combined actuator output with the co-flow stream activated.

Downloaded by John Solomon on July 15, 2023 | http://arc.aiaa.org | DOI: 10.2514/6.2023-4240

Acknowledgments

The National Science Foundation has provided partial support for this work to UTSI through Tuskegee University on grant number 1900177. The authors would like to thank Jamison Murphree and Daniel Allen for their assistance in the execution of experiments.

References

[1] Solomon, J. T., "Liquid Jet Blasting Using Ultra-High Frequency Supersonic Pulsed Air Jet," *Journal of Flow Control, Measurement & Visualization*, Vol. 10, No. 2, 2022, pp. 57–75.

[2] Solomon, J. T., and Nayak, C., "Resonance Enhanced Microactuator (REM) Nozzles for Supersonic Flow Mixing," *47th AIAA Fluid Dynamics Conference*, 2017, p. 4308.

[3] Solomon, J. T., Kreth, P. A., Lockyer, R., and Jones, T., "High-Frequency Pulsed Co-axial Injectors for High-Speed Flow Mixing and Control," *AIAA AVIATION 2022 Forum*, 2022, p. 3926.

[4] Kreth, P. A., Ali, M. Y., Fernandez, E. J., and Alvi, F. S., "Velocity field measurements on high-frequency, supersonic microactuators," *Experiments in Fluids*, Vol. 57, No. 5, 2016, pp. 1–13.

[5] Gragston, M., Price, T. J., Davenport, K., Schmisseur, J. D., and Zhang, Z., "An m by n FLDI array for single-shot multipoint disturbance measurements in high-speed flows," *AIAA Scitech 2021 Forum*, 2021, p. 0599.

[6] Price, T. J., Gragston, M., Schmisseur, J. D., and Kreth, P. A., "Measurement of supersonic jet screech with focused laser differential interferometry," *Appl. Opt.*, Vol. 59, No. 28, 2020, pp. 8902–8908.

[7] Solomon, J. T., Caines, K., Nayak, C. R., Jones, M., and Alexander, D., "Design and Characterization of Nozzle-Injection Assemblies Integrated with High-Frequency Microactuators," *AIAA Journal*, Vol. 56, No. 9, 2018, pp. 3436–3448.

[8] Solomon, J., Hackworth, N., Lockyer, R., Philip, U., and Kreth, P., "Velocity and Vorticity Fields of a High-Frequency Pulsed Supersonic Co-Axial Injector," *AIAA Aviation 2023 Forum*, 2021.

[9] Gragston, M., Siddiqui, F., and Schmisseur, J. D., "Detection of second-mode instabilities on a flared cone in Mach 6 quiet flow with linear array focused laser differential interferometry," *Experiments in Fluids*, Vol. 62, 2021, pp. 1–12.

[10] Hou, Y., *Particle image velocimetry study of shock-induced turbulent boundary layer separation*, The University of Texas at Austin, 2003.

[11] Kocher, B. D., Kreth, P. A., Schmisseur, J. D., LaLonde, E. J., and Combs, C. S., "Characterizing Streamwise Development of Surface Roughness Effects on a Supersonic Boundary Layer," *AIAA Journal*, Vol. 60, No. 9, 2022, pp. 5136–5149.

[12] Adrian, R. J., and Westerweel, J., *Particle image velocimetry*, 30, Cambridge university press, 2011.

[13] Wieneke, B., "PIV uncertainty quantification from correlation statistics," *Measurement Science and Technology*, Vol. 26, No. 7, 2015, p. 074002.

Downloaded by John Solomon on July 15, 2023 | http://arc.aiaa.org | DOI: 10.2514/6.2023-4240